

## FLOW SIMULATION OF THE HISMELT PROCESS

Mark P. DAVIS<sup>1</sup> Rod J. DRY<sup>2</sup> and M. Philip SCHWARZ<sup>3</sup>

<sup>1</sup> Rio Tinto Technical Services, WA 6837, AUSTRALIA

<sup>2</sup> Hismelt Corporation, Kwinana, WA 6966, AUSTRALIA

<sup>3</sup> CSIRO Minerals, Clayton, Victoria 3169, AUSTRALIA

### ABSTRACT

Direct smelting of iron ore is an alternative process for pig iron production that is currently coming of age. The Hismelt Direct Ironmaking Process, after a 20-year development phase, is rapidly emerging as a viable alternative to the traditional blast furnace route. Rio Tinto, together with Nucor Steel, Mitsubishi and Shougang Steel as JV partners, is now in the process of building a 0.8 Mt/a plant in Western Australia.

Hismelt uses iron ore and coal fines directly by injecting them into a molten bath at high velocity. Smelting gases (mainly CO) are released from the bath and burned in the topspace by hot, oxygen-enriched air. A fountain of metal and slag erupts from the bath and, as droplets and splashes traverse through the topspace, they carry heat back to the bath to sustain the process. This "heat pump" is the heart of the Hismelt process.

A major enabling step in the development of the process is understanding the fluid dynamics involved together with the associated heat and mass transfer processes. Hismelt initiated CFD studies in the mid 1980's and has continuously refined this capability. The flow models developed are regarded within Hismelt as major risk-management tools with considerable predictive power in terms of scale-up and process optimisation.

This paper describes one of the flow models that have been developed and provides an example of its use in process development, understanding and scale-up.

### NOMENCLATURE

$a$	absorption coefficient
$A_p$	projected area
$C_d$	drag coefficient
$C_p$	heat capacity
$d$	diameter
$\mathbf{g}$	acceleration due to gravity
$h$	heat transfer coefficient
$h_D$	droplet mass transfer coefficient
$k$	thermal conductivity
$k_r$	surface reaction rate
$m_d$	droplet mass
$\dot{N}_i$	molar flux of species $i$
$P$	pressure
$\dot{q}$	heat flux

$R$	universal gas constant
$Re$	Reynolds number
$S_\phi$	source term for variable $\phi$
$St$	Stanton number
$T$	temperature
$t$	time
$\mathbf{u}$	velocity
$V_{slip}$	gas-droplet slip velocity
$We$	Weber number
$Y_{i,b}$	species $i$ concentration in the bulk

### Greek Symbols

$\delta$	layer thickness
$\varepsilon_w$	wall emissivity
$\phi$	conserved variable
$\Gamma_\phi$	exchange coefficient for variable $\phi$
$\mu$	dynamic viscosity
$\rho$	density
$\sigma_s$	scattering coefficient
$\sigma$	Stefan-Boltzmann constant

### Subscripts

$c$	critical	$liq$	liquidus
$cnv$	convection	$out$	outflow
$d$	droplet	$rad$	radiation
$g$	gas	$s$	slag
$in$	inflow	$w$	wall
$l$	layer	$wcp$	water-cooled panel

### INTRODUCTION

Direct smelting has been talked about for a long time, but has been slow in coming to fruition. In recent times the incentive has intensified due to increased environmental pressure associated with blast furnace ironmaking. However, the process development task is a difficult one, with scale-up presenting the greatest challenge and leading to many disappointments.

A 20-year development phase, involving multiple pilot plants, culminated in a 2.7 m ID vertical smelter being built in 1996 and commissioned in 1997. This plant surpassed all expectations during its two years of operation, both in terms of process performance and engineering availability. Commercialisation of the process has now proceeded to the stage where the JV partners are now in the process of building a Hismelt plant at Kwinana in Western Australia. The plant has a 6 m ID smelter and will have a production capacity of 0.8 Mt/a pig iron. Start-up is scheduled for late 2004.

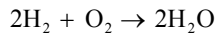
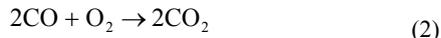
Understanding and harnessing the complex fluid dynamics associated with the process has taken time and has only become possible, through the application of Computational Fluid Dynamics (CFD), quite recently. HIsmelt initiated CFD modelling work with CHAM Ltd and the CSIRO in the mid 1980's, each group investigating different aspects of the process. More recently the modelling work has been performed by Rio Tinto Technical Services. The flow modelling work that has been performed over these years has helped demystify the behaviour of the process to the point where full commercial implementation now is possible with a high degree of confidence.

### Process Description

The HIsmelt process, depicted in Figure 1, involves high-velocity injection of solids (coal, iron ore and fluxes) into a molten iron bath at around 1450 °C. Injection is arranged such that significant penetration of solids into the iron bath is achieved leading to the dissolution of carbon into the metal and the reduction of iron ore via the overall reaction:



This reaction is highly endothermic and, if the process is to be sustained, an external supply of heat is needed. Carbon monoxide (plus hydrogen) released from the bath provides the fuel for generating this heat. Hot blast (1200 °C, oxygen-enriched air) is injected into the topspace via a central swirl lance and combustion takes place to burn the bath gases to carbon dioxide and water.



Theoretically one would like to achieve total combustion of this bath gas but, in practice, post-combustion of around 50-60% is typically achieved. Post-combustion (PC) is defined as the ratio of the volumetric concentration of combusting species, viz:

$$\text{PC}(\%) = 100(\text{CO}_2 + \text{H}_2\text{O})/(\text{CO} + \text{CO}_2 + \text{H}_2 + \text{H}_2\text{O}) \quad (3)$$

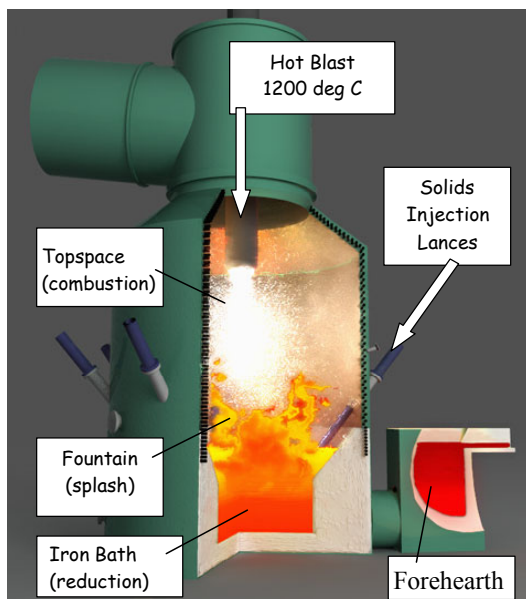


Figure 1: The HIsmelt Process

Smelting occurs in the melt where the oxygen potential is low, whereas heat generation occurs in the topspace where oxygen potential is relatively high. The key to the process is moving heat from the combustion region down to the smelting region without compromising the oxygen potential in either zone.

When CO and H<sub>2</sub> are released from smelting in the bath, the rate of release is such that a violent eruption of liquid is produced. Metal and slag are thrown upward forming a gas-permeable fountain with high surface area for heat transfer. Hot combustion gases pass through this fountain and, in doing so, transfer heat to the droplets of slag and metal which in turn deliver this heat to the bath.

Metal leaves the vessel continuously via an overflow forehearth (which is effectively a liquid metal manometer seal), whereas slag is tapped periodically through the side-wall of the vessel via a water-cooled slag notch.

### HIsmelt Flow Models

Two CFD models have been developed to simulate the HIsmelt process, the Bath Model and the Topspace Model. As the names imply, these models cover the lower and upper regions of the vessel respectively. As described elsewhere, e.g. Davis et al (2003), this division is artificial and is made so that flow simulations can be performed in a reasonable timeframe. As the bath model is a three dimensional, dynamic, 2-phase Eulerian model that incorporates both Lagrangian tracking and the Algebraic Slip Model to model the bath smelting process, simulation times can be excessive. Conversely, the topspace model, described in detail below, requires only moderate execution times and has therefore been used extensively in process optimisation and scale-up.

### TOPSPACE MODEL DESCRIPTION

The topspace model simulates the flow of gas, liquid droplets and particles in the volume above the iron and slag bath. Account is taken of the inflow of hot blast and bath gases, the formation of a droplet fountain above the bath surface, the flow and combustion of char and soot particles, heat transfer to the vessel walls, and radiation. The model includes the effects of droplet breakup, droplet decarburisation by process gases, and droplet heat transfer.

The CFD code PHOENICS has been used as the framework for model development. A two-dimensional axi-symmetric model is generally used for process simulations, although a three-dimensional version of the model has also been built. More recently the model has been ported into the Physica code to enable the simulation of more complex process configurations (Bailey, 1999).

The equations describing the steady-state, turbulent, non-isothermal flow in the vessel are characterised by the following partial differential equation, which represents the transport of a generic conserved variable  $\phi$  under the influence of a source  $S_\phi$ :

$$\nabla \cdot (\rho \mathbf{u} \phi - \Gamma_\phi \Delta \phi) = S_\phi \quad (4)$$

The conserved variables in the topspace model are mass, momentum, gas enthalpy, three mixture fractions, the turbulence variables  $k$  and  $\epsilon$ , composite radiosity, and the mass fraction and shadow mass fraction of soot and char.

## Boundary Conditions

### Hot Air Blast

The HAB lance consists of an annulus through which pre-heated oxygen enriched air travels. The flowrate, composition, and temperature of this flow are taken from HIs melt flowsheet calculations.

Prior to entering the topspace the blast flows through vanes which impart swirl to the flow. This increases jet entrainment and hence combustion. Heat generation within the topspace is thereby improved, and the extent to which blast oxygen can decarburise the fountain droplets is reduced.

It is well recognised that the standard isotropic  $k-\epsilon$  model of turbulence does not model swirl well due to the anisotropic nature of the turbulence. The Reynolds-stress model would be a more accurate turbulence model in this situation, however, its numerical robustness and computational expense makes it an impractical model for industrial CFD. A hybrid turbulence model has therefore been implemented, based on work of Frith and Duggins (1985). This model accounts for the anisotropic turbulent stress distribution by assigning a turbulent viscosity based on a Prandtl mixing length to the swirl momentum equation, and a viscosity evaluated in the standard  $k-\epsilon$  manner to the axial and radial momentum equations (as well as all other dependent variables). This approach has been validated by comparison with data obtained from physical modelling studies performed at the CSIRO (Davis, 1998).

### Bath gas

Under equilibrium conditions the highly reducing well-mixed bath is assumed to produce only CO and H<sub>2</sub> together with conveying N<sub>2</sub>. The rate of production of these gases depends on the overall smelting rate of the process which is a function of the net heat transfer to the bath from the topspace. A mass and energy balance around the bath is therefore required to close this loop. This balance is shown schematically in Figure 2.

The bath model functionality is provided by linking with a library containing a dynamic, lumped, mass & heat balance model of the vessel. The model is written in C++ and incorporates numerical solvers to allow the user-application (in this case the CFD topspace model) to programmatically formulate the problem to be solved.

In this case, the bath model is configured with assays of feed materials and the desired operating composition of the bath (e.g. slag basicity, metal carbon). The topspace model provides the total heat flow to the bath,  $Q_{\text{bath}}$ , which mainly comprises the convective and radiative heat flux to the fountain droplets, and the flow of carbon into the topspace. The latter is in the form of CO from droplet decarburisation, as well as soot and char particles. The bath model then generates the corresponding bath gas rate and composition (as well as the injected feed rates and production rates of metal and slag).

In this manner the topspace model is able to provide a prediction of the overall production rate for the process for a fixed HAB rate and constant inventory of metal and slag.

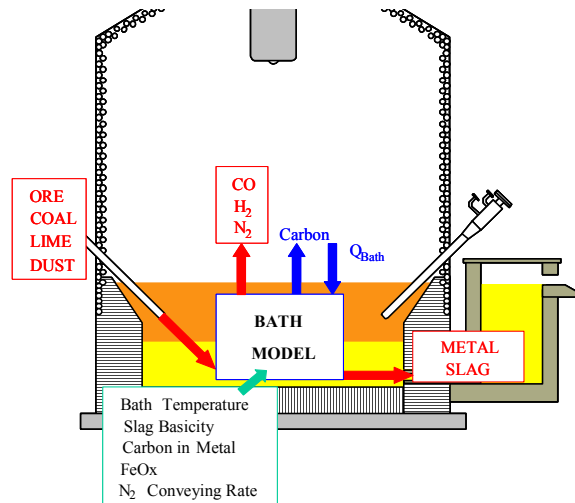


**Figure 2:** Calculation of bath performance.

The bath surface is located from a knowledge of the metal and slag inventory, and from the assumed bulk density of these phases within this highly agitated bath. However, this is an artificial boundary, in reality there is a significant turnover of the bath in the form of liquid fingers and droplets arising from the high rate of bath gas generation.

### Wall heat flux

The modelling of the wall heat flux is crucial to the overall heat balance and the prediction of process performance. Vessel walls comprise water-cooled panels (WCP's) and refractory, both of which are likely to have a coating of solidified slag. Lower down in the vessel there will be a continuous stream of liquid falling down the barrel wall due to fountain splash, as depicted in Figure 3.

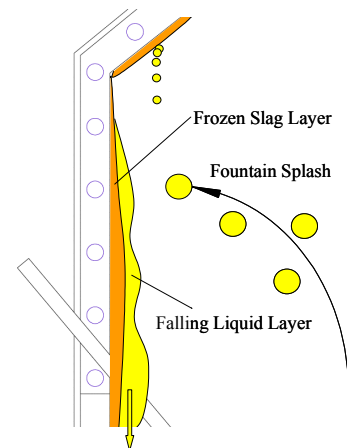


**Figure 3:** Barrel-wall conditions.

Given these wall conditions, a wall heat transfer model has been formulated which takes into account the existence of a frozen slag layer and a falling liquid layer.

Assuming thermal equilibrium through the various wall layers, the following energy balance can be written:

$$\begin{aligned} \dot{q}_{wcp} &= \frac{k_s}{\delta_s} (T_{liq} - T_{wcp}) = h_l (T_l - T_{liq}) \quad (5) \\ &= \dot{q}_{rad} + \dot{q}_{cnv} \end{aligned}$$

This balance assumes that the slag surface is at the liquidus temperature. The convective heat transfer coefficient,  $h_l$ , is calculated according to the correlation of Wilke (1962) which provides a Nusselt number as a function of the layer Reynolds and Prandtl numbers. A layer width and velocity is therefore required (in addition to the layer properties). These are calculated from standard equations for laminar flow of a falling film, viz.:

$$\mathbf{u}_l = \frac{\rho_l \mathbf{g} \delta_l^2}{3 \mu_l} \quad (6)$$

together with a one-dimensional mass balance that takes into account the mass flow of droplets impinging on the wall at any particular height.

The solution of these equations is completed by performing an energy balance over each control volume of the liquid layer:

$$\dot{q}_{in} + \dot{q}_d + \dot{q}_{rad} + \dot{q}_{env} = \dot{q}_{wcp} + \dot{q}_{out} \quad (7)$$

For flow where convective heat transfer (between the layer and frozen slag) dominates, the surface temperature of the layer can be taken as being equal to the bulk temperature. Thus equation (7) provides an equation for the bulk temperature of the layer, which is solved by Newton's method.

Higher up the barrel wall, lower splash flows result in only intermittent formation of a liquid layer, but, over time, a slag layer builds up until the slag surface is at the liquidus temperature. To model this intermittency, a linear variation between liquidus temperature and the calculated layer temperature, as a function of splash flowrate, is assumed for the wall temperature. This modification greatly improves the comparison between model predictions and plant data.

The wall model reveals that close to the bath heat transfer to the WCP's is determined by convective heat transfer between the falling layer and the frozen slag. The high flowrate of liquid down the wall resulting in a layer temperature that is close to bath temperature. Higher up the wall heat flux is dominated by radiation from the process.

For walls above the vessel barrel, wall heat transfer is modelled using equation (8), where the wall heat transfer coefficient is taken from plant measurements, and the slag surface temperature is not allowed to fall below the liquidus temperature.

$$\dot{q}_{wcp} = h_w (T_w - T_{wcp}) = \dot{q}_{rad} + \dot{q}_{env} \quad (8)$$

The convective heat transfer to the walls is calculated using the generalised logarithmic wall function method of Launder and Spalding (1974), wherein a Stanton number is derived and used to calculate the convective heat flux from the gas, viz:

$$\dot{q}_{env} = St C_p \rho_g \mathbf{u}_g (T_g - T_w) \quad (9)$$

The radiative heat flux is calculated using equation (23). Equation (8) is again solved using Newton's method to yield the wall temperature.

## Droplet Fountain

A standard Lagrangian particle tracking approach is used to track droplet motion through the topspace. The standard droplet momentum equation is solved, viz:

$$m_d \frac{d\mathbf{u}_d}{dt} = m_d \mathbf{g} - 0.5 \rho_g A_p C_d V_{slip}^2 \quad (10)$$

where the drag coefficient is that for a sphere (Clift et al, 1978). Equation (10) is cast in finite-difference form to reduced execution time. Over 90 000 tracks are launched from the bath surface in order to obtain sufficient coverage of the volume above the bath. A smaller number would potentially result in an uneven distribution of interphase source terms, especially where the grid is fine, leading to poor convergence of the simulation.

The initial conditions of each track at the bath surface are determined using simulation results of the CFD bath model scaled using 'fountain correlation' values for fountain mass, height and other quantities as a function of vessel operating conditions. These correlations consist of semi-empirical equations developed from consideration of bath penetration by solid-laden jets (Farias and Irons, 1985), and fountain creation by gas buoyancy (Schwarz, 1991). In this manner the CFD bath model does not have to be run in conjunction with every topspace simulation. This would be impractical due to the long execution times that are required.

Given the high aerodynamic force the HAB jet can exert on the fountain, droplet breakup will occur when larger droplets travel into the jet. A droplet breakup model has therefore been developed from the comprehensive review of fragmentation dynamics by Kolev (1993). In this model a critical Weber number is calculated to determine if the droplet is in a region where it is unstable, equation (11).

$$\begin{aligned} Re_d < 200 & \quad \text{Droplet Stable} \\ Re_d > 2000 & \quad We_c = 5.28 \\ \text{otherwise} & \quad We_c = 36 \left( \frac{24}{Re_d} + \frac{20.1807}{Re_d^{6.15}} - \frac{16}{Re_d^{7.5}} \right) \end{aligned} \quad (11)$$

If the droplet Weber number is greater than the critical value, the droplet will be subject to vibrational effects but will not immediately fragment. A delay is therefore calculated which accounts for the time required to undergo complete fragmentation.

$$t_{frag} = \frac{2.3 We_d^{2.5} d_d \left( \frac{\rho_d}{\rho_g} \right)^5}{\mathbf{u}_g} \quad (12)$$

Given the range of Weber number encountered in the topspace, bag breakup is the expected mode of breakup. With this mode a thin hollow bag is blown downstream attached to a toroidal rim. Breakup results in a few large droplets, from the rim, and a large number of tiny droplets from the bag. A mean droplet size after breakup is calculated which assumes 70% of the mass breaks into 5 droplets and the rest into 65 droplets. A more accurate model would commence tracking the two droplet sizes separately, but this has not been implemented due to its computational expense.

Decarburisation of iron droplets occurs in the topspace through surface reactions with carbon dioxide, water and

oxygen to produce carbon monoxide and hydrogen. This is known as back-reaction as it goes against the post combustion reactions that are generating topspace smelting energy. The modelled reactions are:



For decarburisation of iron droplets, the kinetics of oxygen reaction at the droplet surface are considered to be fast and are therefore neglected. On this basis the decarburisation rate can be derived from the diffusive flux to the surface:

$$\dot{N}_i = h_D \left( \frac{P}{RT} \right) \ln[1+Y_{i,b}] \quad (16)$$

The mass transfer coefficient is calculated from the Sherwood number using standard empirical correlations found in the literature (Rowe et al, 1965).

The flux of carbon dioxide and water to a droplet surface is assumed equal to the reactive flux, and the net flux given by Nagasaka and Fruehan (1994) is approximated to:

$$\dot{N}_i = \frac{P Y_{i,b}}{\left[ \frac{RT}{h_D} + \frac{1}{k_r} \right]} \quad (17)$$

From the experimental work of these authors the surface reaction rate is given by:

$$k_r = \frac{k^o}{1 + K_s \gamma_s [pctS]} + k_{res} \quad (18)$$

The same source is used to evaluate the variables in equation (18) as a function of bath temperature for both carbon dioxide and water.

Measurements of decarburisation by both Fruehan and Belton (e.g. Sain and Belton, 1978) have shown it to be first order with respect to the partial pressure of CO<sub>2</sub> and H<sub>2</sub>O and provide evidence that the rate limiting step is the dissociation of these species on the droplet surface. Further discussion of droplet reaction mechanisms is given in Cusack (1991).

Convective heat transfer between the droplets and the gas is calculated using standard empirical relations based on the droplet Nusselt number.

### Soot and Char

The soot and char model is designed to capture only the gross effects of this particulate phase on the dynamics of the topspace. As the particle size and volume fraction are small, a no-slip condition between gas and particle is assumed. This enables transport through the topspace to be modelled simply by the solution of a conserved scalar, equation (4), with  $\phi$  as the particulate concentration.

The only impact the soot and char phase has on the dynamics of the topspace is through the combustion and gasification reactions that result in the transfer of energy to the gas phase, as well as a transfer of carbon in the form of CO (reactions 13 to 15).

The kinetics of oxidation are fast, and therefore the combustion rate is calculated assuming mass transfer

control in a similar manner to droplet decarburisation by oxygen.

Gasification by CO<sub>2</sub> and H<sub>2</sub>O takes place under either reaction control or pore diffusion control. A kinetic rate expression has been adopted from experiments by the CSIRO of CO<sub>2</sub> reactivity of H<sub>2</sub>smelt char and takes the form:

$$\dot{N}_{\text{CO}_2} = k_r (P Y_{\text{CO}_2,s})^{0.6} \quad (19)$$

Assuming the reaction rate is equal to the diffusion rate of CO<sub>2</sub> yields the following equation:

$$\dot{N}_{\text{CO}_2} \frac{RT}{h_D} + \left( \frac{\dot{N}_{\text{CO}_2}}{k_r} \right)^{1/0.6} = P Y_{\text{CO}_2,b} \quad (20)$$

which is solved by Newtons method. An Arrhenius expression has been adopted for the reaction rate using the CSIRO data. The mass transfer coefficient again takes the standard form for spherical particles.

The particle diameter is derived using the ‘shadow’ technique of Spalding as extended by Fueyo (1997) and others. In this technique an additional conserved scalar equation for the particulate phase is solved which is identical to the original equation, but does not contain the mass transfer effects of combustion. Given that the number of particles remains constant it can be shown that:

$$\frac{\phi_{\text{shadow}}}{\phi} = \frac{\text{uncombusted mass}}{\text{combusted mass}} = \left( \frac{d_i}{d} \right)^3 \quad (21)$$

from which the particle diameter can be calculated. The ‘original’ diameter,  $d_i$ , is taken as the representative diameter of the particles at the bath surface. For recirculating flow, such as exists in the topspace, there will be a range of particle sizes in each computational cell as a result of upstream combustion. The diameter given by equation (21) can therefore be considered as providing an average diameter in each cell.

### Combustion

Gas phase combustion in the topspace is modelled using the CREK program (Gordon and M<sup>c</sup>Bride, 1971). In this approach local chemical equilibrium of the gaseous species is assumed and is calculated from the minimisation of the Gibbs free energy function. Moreover, at the temperatures within the topspace this assumes that reactions (2) are fast compared to the turbulent mixing rates.

The transport of enthalpy and three mixture fractions are solved and interfaced with CREK, which then calculates the molar fractions of six species, CO, CO<sub>2</sub>, H<sub>2</sub>, H<sub>2</sub>O, O<sub>2</sub> and N<sub>2</sub> as well as the gas temperature. The ideal gas law is used to calculate the gas density.

### Radiation

Radiation flux within the medium of the topspace is modelled using a composite radiosity equation which represents the net rate of loss or gain of radiant energy per unit volume, equation (22). It has the same form as that used for the irradiance in the P-1 spherical-harmonics approximation to the radiative transfer equation. This model provides reasonable accuracy for optically thick media and can account for scattering and particulate

effects. It is limited to grey radiation, and assumes that all surfaces are diffuse.

$$\nabla \cdot \left( \frac{4}{3(a + \sigma_s)} \nabla \cdot \phi_{rad} \right) + 4a(\sigma T_g^4 - \phi_{rad}) = 0 \quad (22)$$

The absorption and scattering coefficients take account of the various components of the radiative medium, i.e. soot, char and dust particles (these will scatter radiation, as well as absorbing and emitting radiation), CO<sub>2</sub> and H<sub>2</sub>O (both are strong selective absorbers and emitters of radiant energy, but do not scatter), and droplets (these provide additional surfaces that will emit and absorb radiation).

Following from the diffusional slip-boundary condition presented by Diessler (1964) for the Rosseland diffusion model, the heat flux at a wall due to radiation is given by:

$$\dot{q}_{rad} = \frac{2 \varepsilon_w}{(2 - \varepsilon_w)} (\sigma T_w^4 - \phi_{rad}) \quad (23)$$

This model provides reasonable accuracy whilst not incurring the computational expense of more sophisticated models.

## RESULTS

Figures 4 to 6 present simulation results of a process and vessel design that was investigated for operation in North America. The simulation predicts post combustion of 48 % and an offgas temperature of 1420 °C.

The impact of the HAB jet on the droplet fountain is clearly evident in Figure 6 which shows a clear space at the centre where the jet has swept away all droplets. The interaction between the jet and the fountain determines to a large extent the efficiency of the process in terms of heat transfer and post combustion. Combustion of HAB oxygen below the lance can be seen in the gas temperature contours of Figure 5, and, lower down, a larger ‘ball’ of combustion is produced where the jet flows through the droplet fountain. Optimising this interaction is one of the primary uses of the topspace model. If the blast is too close, heat transfer is good but decarburisation of the droplets reduces post combustion and hence available heat. Conversely, pulling the lance away will improve post combustion but also reduce heat transfer, as well as increasing vessel height and wall losses.

The traditional approach to scale-up of metallurgical vessels has been to keep as many ratios as possible constant. Experience with the current model has shown that this can position the lance too close to the fountain leading to insufficient entrainment of process gas for optimal combustion (Davis et al, 2003).

A further use of the model has been to study the impact of slag inventory within the vessel. This will build up between taps, but the overall inventory will also impact on the size and composition of the fountain and hence process performance. Figure 7 shows the impact on gas temperatures of increasing the slag inventory. The available room between lance and bath has been shortened producing a larger combustion region within the fountain and less entrainment of process gas immediately below the HAB lance.

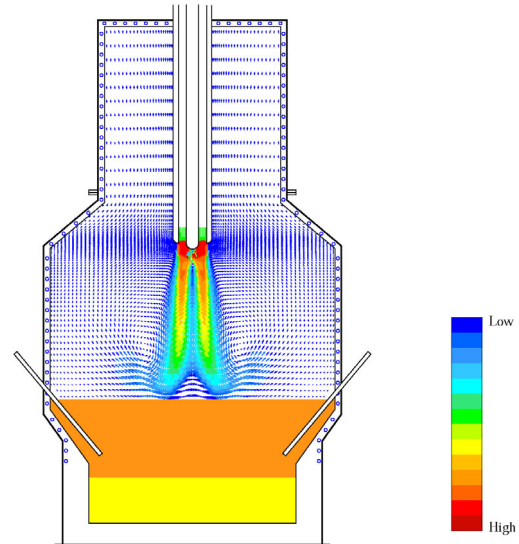


Figure 4: Velocity Vectors.

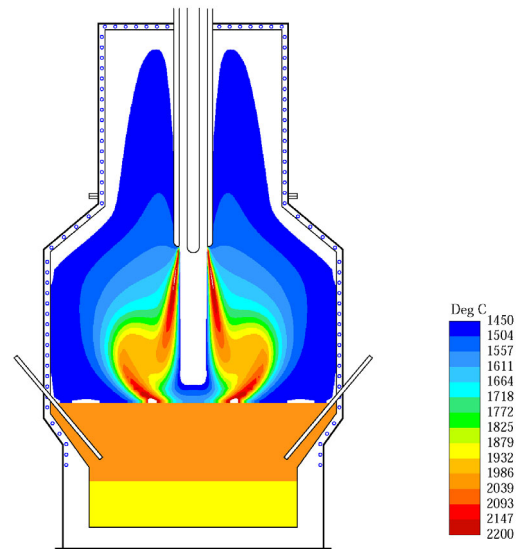


Figure 5: Gas Temperature Contours.

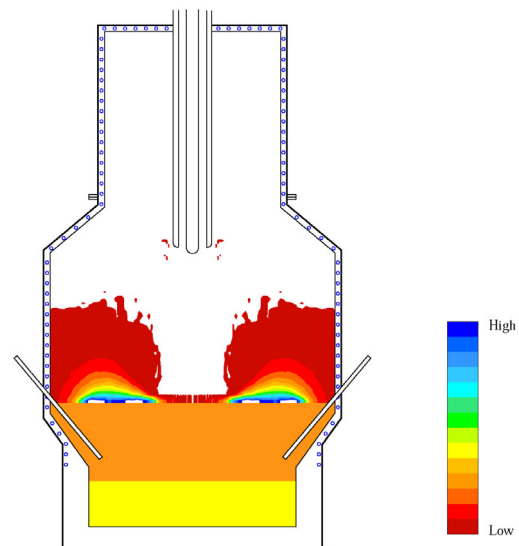
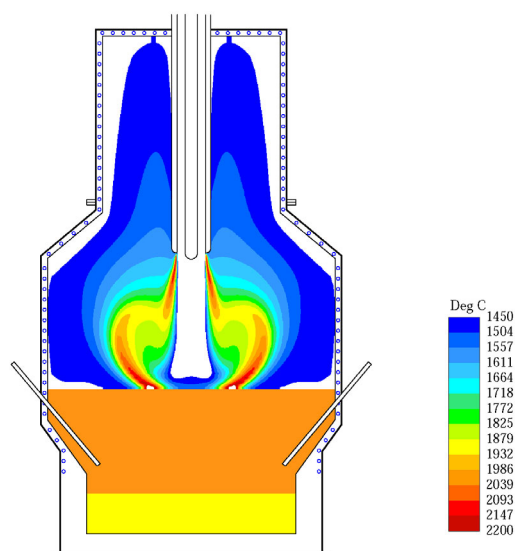


Figure 6: Fountain Concentration Contours.



**Figure 7:** Gas Temperature Contours – increased slag inventory.

An extensive program of model validation has been undertaken in which model predictions have been compared against pilot plant data for a range of plant feed and operating conditions. Given the broad range of physical phenomena that has to be encapsulated within the flow model, the topspace model has performed extremely well. Validation is however an on-going exercise, and will progress when the commercial plant starts production.

## CONCLUSION

After 20 years of pilot plant development the world's first commercial Hismelt plant is under construction in Western Australia. Flow simulation of a broad range of process configurations and vessel designs has played an important part in the scale-up and design exercise. The CFD models that have been developed also provide a means for encapsulating Hismelt's knowledge and understanding of process fundamentals. Further validation of the models and optimisation of the commercial plant will progress once the plant becomes operational later next year.

## REFERENCES

- BAILEY, C., TAYLOR, G.A., CROSS, M. and CHOW, P. (1999) "Discretisation Procedures for Multi-Physics Phenomena", *Journal of Computational and Applied Mathematics*, **103(1)**, 3-17.
- CLIFT, R., GRACE, J.R. and WEBER, M.E., (1978), "Formation and Breakup of Fluid Particles", *Bubbles Drops and Particles*, Academic Press, London, 339-346.
- CUSACK, B.L., HARDIE, G.J. and BURKE, P.D., (1991), "Hismelt – 2<sup>nd</sup> Generation Direct Smelting", *Second European Ironmaking Conf.*, Glasgow.
- DAVIS, M., PERICLEOUS, K., CROSS, M. and SCHWARZ, P., (1998), "Mathematical Modelling Tools for the Optimisation of Direct Smelting Processes", *Applied Mathematical Modelling*, **22(11)**, 921-940.
- DAVIS, M., DRY, R., and SCHWARZ P., (2003), "The Role of CFD Modelling in Development of the Hismelt Process", *ISSTech 2003*, Indianapolis.

DEISSLER, R.G., (1964), "Diffusional Approximation for Thermal Radiation in Gases with Jump Boundary Condition", *ASME J. Heat Transfer*.

FARIAS, L.R. and IRONS, G.A., (1985), "A Unified Approach to Bubbling-Jetting Phenomena in Powder Injection into Iron and Steel", *Met. Trans. B*, **16B**, 211-225.

FRITH, P.W.C. and DUGGINS, R.K., (1985), "Turbulence Modelling of Swirling Flows", *Numerical Methods in Laminar and Turbulent Flow*, Pineridge Press, Swansea, 353-363.

FUEYO, N., BALLESTER, J. and DOPAZO, C., (1997), "The Computation of Particle Size in Eulerian-Eulerian Models of Coal Combustion", *Int. J. of Multiphase Flow*, **23(3)**, 607-612.

GORDON, S. and MCBRIDE B., (1971), "Computer Program for Calculation of Complex Chemical Equilibrium Compositions", *NASA SP-273*.

KOLEV, N.I., (1993), "Fragmentation and Coalescence Dynamics in Multiphase Flows", *Experimental Thermal and Fluid Science*, **6**, 211-251.

LAUNDER, B.E., and SPALDING, D.B., (1974), "The Numerical Computation of Turbulent Flow", *Comp. Meth. In Appl. Mech. And Eng.*, **3**, 269-289.

NAGASAKA, T. and FRUEHAN, R.J., (1994), "Reaction Kinetics of CO<sub>2</sub>-H<sub>2</sub>O Gas Mixtures with Liquid Fe-C Alloys", *ISIJ International*, **34(3)**, 241-246.

ROWE, P.N., CLAXTON, K.T. and LEWIS, J.B., (1965), "Heat and Mass Transfer from a Single Sphere in an Extensive Flowing Fluid", *Trans. Inst. Chem. Eng.*, **41**.

SAIN, D.R. and BELTON, G.R., (1978), "The Influence of Sulphur on Interfacial Reaction Kinetics in the Decarburization of Liquid Iron by Carbon Monoxide", *Met. Trans. B*, **9B**, 403-407.

SCHWARZ, M.P., (1991), "Buoyancy and Expansion Power in Gas-Agitated Baths", *ISIJ International*, **31(9)**, 947-951.

WILKE, W., (1962) "Waermeuebergang an Rieselfilme" (Heat transfer to falling film), *VDI Forschungsheft*, **28**.

